

# Microscopic Theory of the Thermodynamic Properties of $\text{Sr}_3\text{Ru}_2\text{O}_7$

Wei-Cheng Lee<sup>1,\*</sup> and Congjun Wu<sup>1,†</sup>

<sup>1</sup>*Department of Physics, University of California, San Diego, California, 92093, USA*

(Dated: October 30, 2018)

The thermodynamic properties of the bilayer  $\text{Sr}_3\text{Ru}_2\text{O}_7$  at very low temperatures are investigated by a realistic tight-binding model with the on-site interactions treated at the mean-field level. Due to the strong spin-orbit coupling, the band structure undergoes a significant change in Fermi surface topology as the external magnetic field is applied, invalidating the rigid band picture in which the Zeeman energy only causes chemical potential shifts. In addition, since  $\text{Sr}_3\text{Ru}_2\text{O}_7$  is a  $t_{2g}$  active system with unquenched orbital moments, the orbital Zeeman energy is not negligible and plays an important role in the phase diagram on the magnetic field orientation. We find that both the total density of states at the Fermi energy and the entropy exhibit a sudden increase near the critical magnetic field for the nematic phase, echoing the experimental findings. Our results suggest that extra cares are necessary to isolate the contributions due to the quantum criticality from the band structure singularity in this particular material. The effects of quantum critical fluctuations are briefly discussed.

PACS numbers: 72.80.Ga, 73.20.-r, 71.10.Fd

## I. INTRODUCTION

Recently, a great deal of attention has been paid to the bilayer ruthenate compound  $\text{Sr}_3\text{Ru}_2\text{O}_7$  with various interesting physical properties. It was first considered as a field-tuned quantum critical state having metamagnetic transitions around 8 Tesla<sup>1-3</sup>. Later, in the ultra-pure single crystal it has been found that the metamagnetic quantum critical point is intervened by the emergence of an unconventional anisotropic (nematic) electronic state<sup>4,5</sup>, stimulating considerable theoretical efforts<sup>6-18</sup>.  $\text{Sr}_3\text{Ru}_2\text{O}_7$  is a metallic itinerant system with the active  $t_{2g}$ -orbitals of the Ru sites in the bilayer  $\text{RuO}_2$  ( $ab$ ) planes. At very low temperatures ( $\sim 1\text{K}$ ), it starts as a paramagnet at small magnetic fields. Further increasing field strength leads to two consecutive metamagnetic transitions at 7.8 and 8.1 Tesla if the field is perpendicular to the  $ab$ -plane. The nematic phase is observed between these two transitions, identified by the observation of anisotropic resistivity without noticeable lattice distortions.

This nematic phase in  $\text{Sr}_3\text{Ru}_2\text{O}_7$  can be understood as the particle-hole channel Fermi surface instability of the Pomeranchuk-type<sup>3</sup>. It is a mixture of the  $d$ -wave Pomeranchuk instabilities in both density and spin channels<sup>19</sup>, though the microscopic origin of these instabilities remain controversial. Different microscopic theories have been proposed based on the quasi-1D bands of  $d_{xz}$  and  $d_{yz}$ <sup>14,15,18</sup>, and based on the 2d-band of  $d_{xy}$ <sup>8,9,16,17</sup>. In our<sup>14,18</sup> and Raghu *et. al.*'s<sup>15</sup> theories, the unconventional (nematic) magnetic ordering was interpreted as orbital ordering among the  $d_{xz}$  and  $d_{yz}$ -orbitals. In particular, in Ref. [18] a realistic tight-binding model with the important features including the  $t_{2g}$ -orbitals, the bilayer splitting, spin-orbit coupling, and the staggered rotations of  $\text{RuO}$  octahedra, has been derived and shown to reproduce accurately the results of the angle-resolved photon emission spectroscopy (ARPES)<sup>20</sup> and the quasiparticle

interference in the spectroscopic imaging scanning tunneling microscopy (STM)<sup>21</sup>.

On the other hand, orbital physics is an important subject in transition metal oxides with active  $d$ -orbitals<sup>22,23</sup>. Recently the research of orbital physics has been further stimulated due to the observations of anisotropic properties in iron-pnictides<sup>24,25</sup> which are consistent with orbital ordering<sup>26-28</sup>. Generally speaking, a transition metal oxide with active  $t_{2g}$ -orbitals could exhibit orbital ordering in the quasi-1D bands under certain conditions. In the particular case of  $\text{Sr}_3\text{Ru}_2\text{O}_7$ , it has been argued<sup>14,15</sup> that at zero magnetic field, although the system does not show any order, it is near the instabilities of ferromagnetic and orbital (nematic) orderings. Applying the magnetic field pushes the system closer to the van Hove singularities which largely raises up the density of states at the Fermi energy  $\mathcal{D}(\epsilon_F)$  and results in both the metamagnetic and nematic transitions. It should be noted that the Fermi liquid states always dominate the low temperature physics of this system because the resistivity was found to follow  $T^2$  law in both isotropic and nematic phases. This suggests that quantum criticality is not expected to play much role in both isotropic and nematic phases at low temperatures. Nevertheless, quantum critical behavior appears at finite temperatures above the nematic phase, which exhibits non-Fermi liquid properties.

The study of quantum critical states has attracted intensive research activities over past few decades<sup>29,30</sup>. Materials possessing quantum critical points are usually triggered by tunable parameters, for example, external pressure and magnetic field. When approaching quantum critical points, not only the zero temperature electronic ground state but also the low-temperature properties are modified radically. Pioneering theoretical works done by Hertz<sup>31</sup> and extended by Millis<sup>32</sup> have addressed the physics near the ferromagnetic and antiferromagnetic quantum critical points, showing that the critical fluc-

tuations are scale invariant in the vicinity of quantum critical points due to the divergence of the correlation length right at these points. This aspect enables the establishment of universal classes based on the scaling theory. Experimentally, quantum critical states usually exhibit divergences in thermodynamic properties like specific heat, entropy, *etc.* The critical exponents associated with these divergences are believed to be universal values in the same universal class regardless the microscopic details.

The influence of quantum critical fluctuations in  $\text{Sr}_3\text{Ru}_2\text{O}_7$  seems to be novel as well. Rost *et. al.*<sup>33,34</sup> measured the entropy and specific heat in ultra-pure samples and found divergences near the metamagnetic transitions in both quantities. Although it is a common feature in a quantum critical state that the specific heat  $C$  diverges as  $C/T = A[(H - H_c)/H_c]^{-\alpha} + B$  due to quantum fluctuations, the exponent of  $\alpha$  is fitted to be 1 instead of  $1/3$  as predicted by the Hertz-Millis theory<sup>31,32</sup>. The total density of states (DOS) measured by Iwaya *et al.*<sup>35</sup> using the STM showed that the DOS at the Fermi energy ( $\mathcal{D}(\epsilon_F)$ ) increases significantly under the application of the magnetic field, but the DOS at higher and lower energy does not change accordingly. This indicates that the Zeeman energy in this case does not simply cause a chemical potential shift so that the conventional rigid band picture can not explain this result. These findings have posted a challenge to understand the critical behavior in this material.

In this article, we show that the tight-binding model derived by Arovas and two of us<sup>18</sup> together with the on-site interactions treated simply at the mean-field level already gives rise to divergences in these properties without involving quantum fluctuations. Realistic features like multi-orbital bands, the bilayer splitting, the rotations of RuO octahedra, and spin-orbit coupling make this material very sensitive to small energy scales. Because parts of the Fermi surface are close to the van Hove singularities, Fermi surface reconstructions in the external magnetic fields lead to a singular behavior in  $\mathcal{D}(\epsilon_F)$ . This results in the divergences observed in the experiments mentioned above. Because of the strong spin-orbit coupling and the unquenched orbital moments, the Zeeman energy tends to reconstruct the Fermi surfaces rather than just provides a chemical potential shift. Our results suggest that the influence of quantum critical fluctuations will be masked if  $\mathcal{D}(\epsilon_F)$  of the system exhibits a non-monotonic behavior with the tuning parameters, implying that a more careful analysis is required in order to distinguish the role of the quantum criticality in the bilayer  $\text{Sr}_3\text{Ru}_2\text{O}_7$ .

This paper is organized as follows. We will summarize the tight-binding model derived in Ref. [18] in Sect. II. The formalism of the mean-field theory will be presented in Sect. III. The results for the cases of the magnetic fields parallel to and tilted away from the  $c$ -axis will be discussed in Sect. IV and V, respectively. Conclusions will be given in Sect. VI.

## II. THE TIGHT-BINDING MODEL

The detailed band structure of  $\text{Sr}_3\text{Ru}_2\text{O}_7$  is complicated by the  $t_{2g}$ -orbital structure (e.g.  $d_{xz}, d_{yz}, d_{xy}$ ), the bilayer splitting, the staggered distortion of the RuO octahedra, and spin-orbit coupling. We have constructed a detailed tight-binding Hamiltonian which gives rise to band structures in agreement with the ARPES data in a previous work<sup>18</sup>. We found that a difference of the on-site potential between the two adjacent RuO layers,  $V_{\text{bias}}$ , should be added<sup>18</sup> in order to fit the shape of the Fermi surfaces observed in the ARPES experiments<sup>20</sup>. This term appears because ARPES is a surface probe and this bilayer symmetry breaking effect is important near the surface. Since we focus on the thermodynamic properties which are all bulk properties,  $V_{\text{bias}}$  is set to be zero in this paper. Below we will start from this model and refer readers to Ref. 18 for more detailed information.

The tight-binding band Hamiltonian  $H_0$  can be reduced to block forms classified by  $k_z = 0, \pi$  corresponding to bonding and anti-bonding bands with respect to layers as:

$$H_0 = h_0(k_z = 0) + h_0(k_z = \pi), \quad (1)$$

with  $h_0(k_z)$  defined as

$$h_0(k_z) = \sum_{\vec{k}}' \Phi_{\vec{k}, k_z, s}^\dagger \begin{pmatrix} \hat{h}_{0s}(\vec{k}, k_z) & \hat{g}^\dagger(\vec{k}, k_z) \\ \hat{g}(\vec{k}, k_z) & \hat{h}_{0s}(\vec{k} + \vec{Q}, k_z) \end{pmatrix} \Phi_{\vec{k}, k_z, s}, \quad (2)$$

where the spinor  $\Phi_{\vec{k}, k_z, s}^\dagger$  operator is defined as

$$\Phi_{\vec{k}, k_z, s}^\dagger = \left( d_{\vec{k}, s, k_z}^{yz \dagger}, d_{\vec{k}, s, k_z}^{xz \dagger}, d_{\vec{k}, -s, k_z}^{xy \dagger}, \right. \\ \left. d_{\vec{k} + \vec{Q}, s, k_z}^{yz \dagger}, d_{\vec{k} + \vec{Q}, s, k_z}^{xz \dagger}, d_{\vec{k} + \vec{Q}, -s, k_z}^{xy \dagger} \right); \quad (3)$$

$d_{s, k_z}^\alpha(\vec{k})$  annihilates an electron with orbital  $\alpha$  and spin polarization  $s$  at momentum  $(\vec{k}, k_z)$ ;  $\vec{Q} = (\pi, \pi)$  is the nesting wavevector corresponding to unit cell doubling induced by the rotations of RuO octahedra;  $\sum_{\vec{k}}'$  means that only half of the Brillouin zone is summed. Please note the opposite spin configurations  $s$  and  $-s$  for the  $d_{xz}, d_{yz}$  and  $d_{xy}$ -orbitals in Eq. 3, which is convenient for adding spin-orbit coupling later.

The diagonal matrix kernels  $\hat{h}_{0s}$  in Eq. 2 are defined as

$$\hat{h}_{0s}(\vec{k}, k_z) = \hat{A}_s(\vec{k}) + \hat{B}_1 \cos k_z - \mu \hat{I}, \quad (4)$$

where

$$\hat{A}_s(\vec{k}) = \begin{pmatrix} \epsilon_{\vec{k}}^{yz} & \epsilon_{\vec{k}}^{\text{off}} + is\lambda & -s\lambda \\ \epsilon_{\vec{k}}^{\text{off}} - is\lambda & \epsilon_{\vec{k}}^{xz} & i\lambda \\ -s\lambda & -i\lambda & \epsilon_{\vec{k}}^{xy} \end{pmatrix}, \quad (5)$$

and

$$\hat{B}_1 = \begin{pmatrix} -t_\perp & 0 & 0 \\ 0 & -t_\perp & 0 \\ 0 & 0 & 0 \end{pmatrix}; \quad (6)$$

where  $t_{\perp}$  is the longitudinal inter-layer hopping for the  $d_{xz}$  and  $d_{yz}$  orbitals.  $\lambda$  is the spin-orbit coupling strength which comes from the on-site spin-orbit coupling term as  $H_{so} = \lambda \sum_i \vec{L}_i \cdot \vec{S}_i$ ;  $\mu$  is the chemical potential; the dispersions for the  $d_{yz}$ ,  $d_{xz}$ , and  $d_{xy}$  bands in Eq. 5 are defined as

$$\begin{aligned}\epsilon_{\vec{k}}^{yz} &= -2t_2 \cos k_x - 2t_1 \cos k_y, \\ \epsilon_{\vec{k}}^{xz} &= -2t_1 \cos k_x - 2t_2 \cos k_y, \\ \epsilon_{\vec{k}}^{xy} &= -2t_3 (\cos k_x + \cos k_y) - 4t_4 \cos k_x \cos k_y \\ &\quad - 2t_5 (\cos 2k_x + \cos 2k_y) - V_{xy} \\ \epsilon_{\vec{k}}^{\text{off}} &= -4t_6 \sin k_x \sin k_y,\end{aligned}\quad (7)$$

which includes longitudinal ( $t_1$ ) and transverse ( $t_2$ ) hopping for the  $d_{xz}$  and  $d_{yz}$  orbitals, respectively, as well as nearest neighbor ( $t_3$ ), next-nearest neighbor ( $t_4$ ), and next-next-nearest neighbor ( $t_5$ ) hopping for the  $d_{xy}$  orbital. Following the previous LDA calculations<sup>36</sup>,  $V_{xy}$  is introduced to account for the splitting of the  $d_{yz}$  and  $d_{xz}$  states relative to the  $d_{xy}$  states. While symmetry forbids nearest-neighbor hopping between different  $t_{2g}$  orbitals in a perfect square lattice without the rotation of Ru octahedra, a term describing hopping between  $d_{xz}$  and  $d_{yz}$  orbitals on next-nearest neighbor sites ( $t_6$ ) is allowed and put into the tight-binding model.

The off-diagonal matrix kernel  $\hat{g}(\vec{k}, k_z)$  in Eq. 2 reads

$$\hat{g}(\vec{k}, k_z) = \hat{G}(\vec{k}) - 2\hat{B}_2 \cos k_z, \quad (8)$$

where

$$\hat{B}_2 = \begin{pmatrix} 0 & t_{\text{INT}}^{\perp} & 0 \\ -t_{\text{INT}}^{\perp} & 0 & 0 \\ 0 & 0 & 0 \end{pmatrix}, \quad (9)$$

and

$$\hat{G}(\vec{k}) = \begin{pmatrix} 0 & -2t_{\text{INT}} \gamma(\vec{k}) & 0 \\ 2t_{\text{INT}} \gamma(\vec{k}) & 0 & 0 \\ 0 & 0 & 0 \end{pmatrix}, \quad (10)$$

with  $\gamma(\vec{k}) = \cos k_x + \cos k_y$ .  $t_{\text{INT}}$  and  $t_{\text{INT}}^{\perp}$  describe the intra- and inter-layer hopping between  $d_{xz}$  and  $d_{yz}$  induced by the rotations of RuO octahedra, providing the coupling between  $\vec{k}$  and  $\vec{k} + \vec{Q}$ .

When describing the Zeeman energy, we can choose the magnetic field  $\vec{B}$  to lie on the  $xz$  plane and define  $\theta$  as the angle between  $\vec{B}$  and the  $c$ -axis of the sample without loss of the generality. Consequently, the Zeeman term becomes:

$$\begin{aligned}H_{\text{Zeeman}} &= H_{\text{Zeeman}}^{\text{orbital}} + H_{\text{Zeeman}}^{\text{spin}}, \\ H_{\text{Zeeman}}^{\text{orbital}} &= -\mu_B B \sum_{i,a} (L_{z,ia} \cos \theta + L_{x,ia} \sin \theta), \\ H_{\text{Zeeman}}^{\text{spin}} &= -2\mu_B B \sum_{i,a,\alpha} (S_{z,ia}^{\alpha} \cos \theta + S_{x,ia}^{\alpha} \sin \theta),\end{aligned}\quad (11)$$

where  $a$  is the layer index,  $B = |\vec{B}|$ , and the matrices  $L_{x,z}$  can be found in Ref. [18].

For  $\theta \neq 0$ , the extra Zeeman terms from  $x$ -component of  $\vec{L}$  and  $\vec{S}$  couple  $\Phi_{\vec{k},k_z,\uparrow}^{\dagger}$  and  $\Phi_{\vec{k},k_z,\downarrow}^{\dagger}$ . Defining  $\phi_{\vec{k},k_z}^{\dagger} \equiv (\Phi_{\vec{k},k_z,\uparrow}^{\dagger}, \Phi_{\vec{k},k_z,\downarrow}^{\dagger})$ , the Zeeman term can be written in the matrix form as:

$$H_{\text{Zeeman}} = \mu_B B \sum_{\vec{k}} \sum_{k_z} \phi_{\vec{k},k_z}^{\dagger} \hat{H}_Z(\theta) \phi_{\vec{k},k_z}, \quad (12)$$

where

$$\hat{H}_Z(\theta) = \begin{pmatrix} \hat{H}_Z^D(\theta, +) & 0 & \hat{H}_Z^{O\dagger}(\theta) & 0 \\ 0 & \hat{H}_Z^D(\theta, +) & 0 & \hat{H}_Z^{O\dagger}(\theta) \\ \hat{H}_Z^O(\theta) & 0 & \hat{H}_Z^D(\theta, -) & 0 \\ 0 & \hat{H}_Z^O(\theta) & 0 & \hat{H}_Z^D(\theta, -) \end{pmatrix}, \quad (13)$$

$$\hat{H}_Z^D(\theta, s) = \cos \theta \times \begin{pmatrix} -s & -i & 0 \\ i & -s & 0 \\ 0 & 0 & s \end{pmatrix}, \quad (14)$$

with  $s = \pm 1$  and

$$\hat{H}_Z^O(\theta) = \sin \theta \times \begin{pmatrix} -1 & 0 & 0 \\ 0 & -1 & -i \\ 0 & i & -1 \end{pmatrix}, \quad (15)$$

### III. THE MEAN-FIELD THEORY

In Sect. II, we have introduced the rather complicated band structure of  $\text{Sr}_3\text{Ru}_2\text{O}_7$ . In this section, we introduce the minimal multi-orbital band Hubbard model for the nematic ordering and outline the mean-field procedure.

In realistic band structures measured by ARPES<sup>20</sup>, there exists an additional  $\delta$ -band arising from the  $d_{x^2-y^2}$ -orbital which is not covered by the current model. The particle filling in the  $t_{2g}$ -orbitals is not fixed. For the convenience of calculation, we fix the chemical potential  $\mu = 0.94t_1$  instead of fixing particle filling in the  $t_{2g}$ -orbitals while changing magnetic fields and orientations in Sect. IV and Sect. V. The corresponding fillings inside the  $t_{2g}$ -orbitals per Ru atom varies within the range between 4.05 and 4.06 in Figs. 2, 6, 7. This treatment does not change any essential qualitative physics.

The Hubbard model contains the on-site intra and inter orbital interactions as

$$H_{\text{int}} = U \sum_{i,a,\alpha} \hat{n}_{i\alpha}^{\alpha} \hat{n}_{i\alpha}^{\alpha} + \frac{V}{2} \sum_{i,a,\alpha \neq \beta} \hat{n}_{i\alpha}^{\alpha} \hat{n}_{i\alpha}^{\beta}, \quad (16)$$

where the Greek index  $\alpha$  refers to the orbitals  $xz$ ,  $yz$  and  $xy$ ; the Latin index  $a$  refers to the upper and lower layers. Throughout this paper, the parameter values are taken as  $U/t_1 = V/t_1 = 3.6$ . The other two possible terms

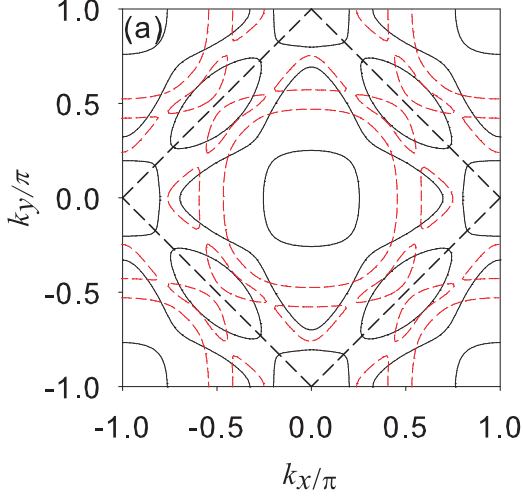


FIG. 1: (Color online) The Fermi surfaces using the bilayer tight-binding model Eq. 2 with the parameters in unit of  $t_1$  as:  $t_2 = 0.1t_1, t_3 = t_1, t_4 = 0.2t_1, t_5 = -0.06t_1, t_6 = 0.1t_1, t_\perp = 0.6t_1, t_{\text{INT}} = t_{\text{INT}}^\perp = 0.1t_1, \lambda = 0.2t_1, V_{xy} = 0.3t_1$ , and  $\mu = 0.94t_1$ . The thick dashed lines mark the boundary of half Brillouin zone due to the unit cell doubling induced by the rotation of RuO octahedra. The Fermi surfaces of the bonding ( $k_z = 0$ , black solid lines) and the anti-bonding bands ( $k_z = \pi$ , red dashed lines) could cross since  $k_z$  is a good quantum number.

in the multi-band Hubbard interaction are the Hund's rule coupling and pairing hopping terms, which do not change the qualitative physics and are neglected. We assume the external  $B$ -field lying in the  $xz$ -plane with an angle  $\theta$  tilted from the  $z$ -axis. The occupation and spin in each orbital and layer are defined as follows:

$$\begin{aligned} n_a^\alpha &\equiv \sum_s \langle d_{s,a}^{\alpha\dagger}(i) d_{s,a}^\alpha(i) \rangle, \\ S_{za}^\alpha &\equiv \frac{1}{2} \sum_s s \langle d_{s,a}^{\alpha\dagger}(i) d_{s,a}^\alpha(i) \rangle, \\ S_{xa}^\alpha &\equiv \frac{1}{2} \sum_s \langle d_{s,a}^{\alpha\dagger}(i) d_{\bar{s},a}^\alpha(i) \rangle. \end{aligned} \quad (17)$$

No any other inter-layer interaction is considered and the non-interacting Hamiltonian has symmetric layers, thus the order parameters are the same for both layers, which have been numerically confirmed. From now on it will be assumed:

$$n_a^\alpha = n^\alpha, \quad S_{x,z a}^\alpha = S_{x,z}^\alpha. \quad (18)$$

With this property,  $k_z$  remains a good quantum number in the resulting mean-field Hamiltonian.

The standard mean-field decomposition of  $H_{\text{int}}$  leads to

$$H_{\text{int}}^{MF} = \sum_{i,a,\alpha} \sum_s W_s^\alpha d_{s,a}^{\alpha\dagger}(i) d_{s,a}^\alpha(i) - U S_x^\alpha d_{s,a}^{\alpha\dagger}(i) d_{\bar{s},a}^\alpha(i), \quad (19)$$

where

$$W_s^\alpha = U \left( \frac{1}{2} n^\alpha - s S_z^\alpha \right) + V \sum_{\beta \neq \alpha} n^\beta. \quad (20)$$

The interaction parameters ( $U, V$ ) are chosen such that no spontaneous magnetization occurs in the absence of the external magnetic field. Moreover, since the order parameters  $\{n_a^\alpha\}$  are non-zero even without magnetic field, we require that the renormalized Fermi surface at zero field to be the one given in Fig. 1. As a result, in addition to the optimized parameters obtained in our previous work<sup>18</sup>, we need to subtract the following term from Eq. 19:

$$H_{\text{shift}} = \sum_{i,a,\alpha} \sum_s W_s^\alpha(0) d_{s,a}^{\alpha\dagger}(i) d_{s,a}^\alpha(i), \quad (21)$$

where

$$W_s^\alpha(0) = \frac{1}{2} U n^\alpha(0) + V \sum_{\beta \neq \alpha} n^\beta(0), \quad (22)$$

and  $n^\alpha(0)$  is the occupation number in orbital  $\alpha$  corresponding to the Fermi surfaces shown in Fig. 1. This is an effect of the renormalization of the chemical potential  $\mu$  and  $V_{xy}$  due to interactions. After putting all the pieces together, we finally arrive at the mean-field Hamiltonian as:

$$\begin{aligned} H^{MF} &= H_0 + H_{\text{int}}^{MF} - H_{\text{shift}} + H_{\text{Zeeman}} \\ &\equiv \sum_{\vec{k}} \sum_{k_z} \phi_{\vec{k}, k_z}^\dagger H^{MF}(\vec{k}) \phi_{\vec{k}, k_z}. \end{aligned} \quad (23)$$

The order parameters are computed self-consistently. It has been pointed out<sup>14,15</sup> that the nematic phase can be identified as the orbital ordering between the  $d_{xz}$  and  $d_{yz}$ -orbitals, thus the nematic order parameter  $\mathcal{N}$  is defined as

$$\mathcal{N} = 2(n^{yz} - n^{xz}). \quad (24)$$

The magnetization order parameter is defined as:

$$\vec{\mathcal{M}} \equiv 2 \sum_{\alpha} \vec{S}^\alpha. \quad (25)$$

The factor of 2 in Eq. 25 and 24 accounts for the double layers.

#### IV. THE CASE OF THE PERPENDICULAR MAGNETIC FIELD ( $\theta = 0$ )

In this section the thermodynamic properties at low temperatures are calculated within the mean-field theory for the case of  $\vec{B} \parallel \hat{c}$ , *i.e.*,  $\theta = 0$ . Most important features of these properties, including the evolution of the nematic ordering, the tunneling DOS, entropy landscapes, and the finite temperature phase diagram under the application of the magnetic field  $B$ , can be reasonably reproduced and understood by the singular behavior of  $\mathcal{D}(\epsilon_F)$  under the magnetic field.

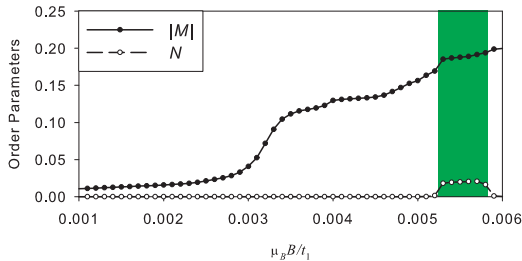


FIG. 2: (Color online) The order parameters as a function of  $\mu_B B$  for  $\theta = 0$ . The nematic phase (in the green area) is bounded by two magnetization jumps which corresponds to metamagnetic transitions.

### A. Nematic ordering and metamagnetic transitions

The order parameters  $|\vec{M}|$  and  $\mathcal{N}$  as functions of  $\mu_B B$  for this case are shown in Fig. 2. There are three rapid increases in the magnetization, consistent with the experiment measurements of the real part of the very low frequency AC magnetic susceptibility at 7.5T, 7.8T and 8.1T, respectively<sup>4</sup>. Experimentally, only the last two exhibit dissipative peaks in the imaginary part of the AC susceptibility, which characterize the first order metamagnetic transitions. The first jump measured in the experiment is considered as a crossover.

The nematic ordering develops in the area bounded by the last two magnetization jumps, reproducing the well-known phase diagram of the  $\text{Sr}_3\text{Ru}_2\text{O}_7$ <sup>4</sup>. In particular, if we adopt the results from LDA calculations<sup>37,38</sup> that  $t_1 \approx 300$  meV, we find that three jumps in the magnetization appear at  $B \approx 0.0032t_1/\mu_B$ ,  $0.0053t_1/\mu_B$ , and  $0.0059t_1/\mu_B \sim 15.7$  T, 26 T, and 29 T, which is within the same order to the experimental values of 7.5T, 7.8T, and 8.1T. This is an improvement compared to the results in previous theory calculations<sup>8–11,15,16</sup>, in which the nematic ordering develops at much higher field strength  $\mu_B B/t_1 \approx 0.02$ .

The sensitivity to the small energy scale like the Zeeman energy is because a part of the Fermi surfaces, mostly composed of quasi-1D bands as shown in the yellow areas in Fig. 3 (b), is getting close to the van Hove singularities at  $(\pi, 0)$  and  $(0, \pi)$ . The evolution of the Fermi surface structures as increasing the B-field across the nematic phase boundaries is presented in Fig. 3 a (before), b (inside), and c (after) at  $\mu_B B/t_1 = 0.0048, 0.00544, 0.006$ , respectively. Before and after the nematic phases, the Fermi surfaces have the 4-fold rotational symmetry as exhibited in Fig. 3 (a) and (c). When the system is in the nematic phase, the Fermi surfaces only have 2-fold symmetry as expected. Particularly, the nematic distortion is most prominent near  $(\pm\pi, 0)$  and  $(0, \pm\pi)$  whose Fermi surfaces are dominated by the quasi-1D bands as shown in Fig. 3(b), supporting the mechanism of orbital ordering in quasi-1D bands

driven by the van Hove singularities.

It is worthy of mentioning that the onsite spin-orbit coupling  $H_{so} = \lambda \sum_i \vec{L}_i \cdot \vec{S}_i$  has important effects on the Fermi surface evolutions.  $H_{so}$  hybridizes the opposite spins between quasi-1D bands  $d_{yz,xz}$  and the 2-D band  $d_{xy}$ . As the spin Zeeman energy is present, the spin majority (minority) bands of  $d_{yz,xz}$  couples to the spin minority (majority) band of  $d_{xy}$ . Moreover, the orbital Zeeman energy provides more hybridizations between quasi-1D  $d_{xz,yz}$  bands. Combined with the above two effects, the addition of the spin and orbit Zeeman energies causes reconstruction of the Fermi surfaces rather than just chemical potential shifts.

These results show that the complexity and the sensitivity of the  $\text{Sr}_3\text{Ru}_2\text{O}_7$  band structure can be captured very well by our tight-binding model with a reasonable quantitative accuracy. In the following, the same model will be used to further investigate some novel physical properties observed in experiments.

### B. Entropy landscape under the magnetic field

One of the intriguing puzzles observed in  $\text{Sr}_3\text{Ru}_2\text{O}_7$  is the critical exponent of the divergence in entropy (as well as specific heat) when approaching the nematic region, or the quantum critical point. Although it is expected that specific heat  $C$  diverges as  $C/T = A[(H - H_c)/H_c]^{-\alpha} + B$  near the quantum critical point, the exponent  $\alpha$  has been found to be 1<sup>33,34</sup> instead of 1/3 as predicted by the Hertz-Millis theory. However, it is noticed that  $\mathcal{D}(\epsilon_F)$  is taken to be a constant in the Hertz-Millis theory while this material has a complicated Fermi surface evolutions under the magnetic field. Moreover, as mentioned in the introduction, the system is always in the Fermi liquid states at low temperatures inferred from the temperature dependences of the resistivity. Motivated by these two facts, it is then worthy of studying first the contribution from the band structure to the entropy before considering the quantum fluctuations.

The entropy per Ru atom at the mean-field level can be evaluated by:

$$S(B) = - \frac{k_B}{N} \sum_{\vec{k}}' \sum_j [f(E_j(\vec{k})) \ln f(E_j(\vec{k})) + (1 - f(E_j(\vec{k}))) \ln(1 - f(E_j(\vec{k})))], \quad (26)$$

where  $\beta = 1/k_B T$ ,  $f(E_j(\vec{k}))$  the Fermi-Dirac distribution function, and  $E_j(\vec{k})$  is the  $j$ th eigenvalue of  $H^{MF}(\vec{k})$  given in Eq. 23. Because only the change of the entropy as a function of magnetic field near the nematic region is experimentally relevant, we plot in Fig. 4 the quantity:  $S(B)/T$  in unit of  $k_B^2/t_1$  at a low temperature of  $1/(\beta t_1) = 0.002$  within the range of  $0.0045 \leq \mu_B B/t_1 \leq 0.007$ . Near the nematic region,  $S(B)/T$  increases first, being cut off inside the nematic region, and then decreases after, which is consistent with the experiment<sup>33</sup>. Since these results are obtained at the mean-field level,

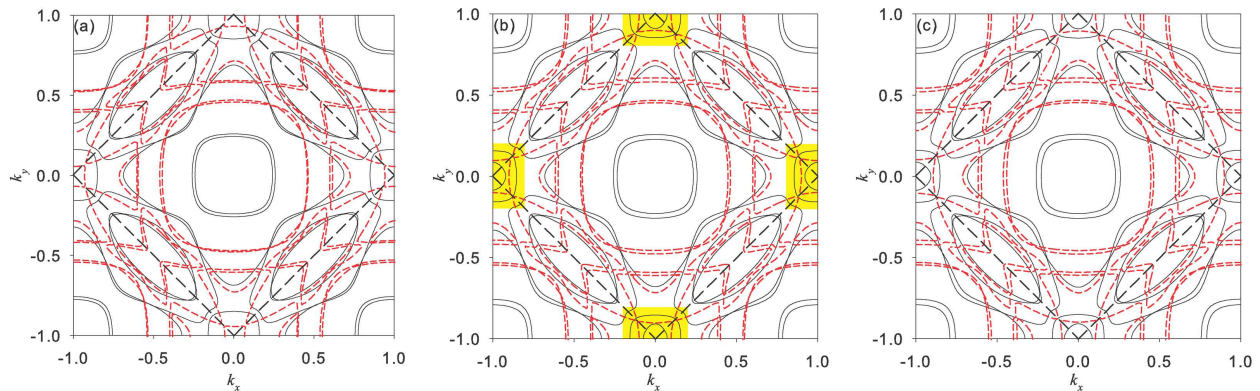


FIG. 3: Fermi surface evolution for the case of magnetic field parallel to  $c$  axis (a) before ( $\mu_B B = 0.0048t_1$ ) (b) inside ( $\mu_B B = 0.00544t_1$ ), and (c) after ( $\mu_B B = 0.006t_1$ ) the nematic phase. Significant changes in the Fermi surface topology under the magnetic field can be seen (see Fig. 1 for the Fermi surfaces at zero field). The nematic distortion is most obvious in the Fermi surfaces near  $(\pm\pi, 0)$  and  $(0, \pm\pi)$  as indicated by the yellow areas in (b). These parts of Fermi surfaces are composed mostly of quasi-1D bands, supporting the intimacy of nematic phase to the orbital ordering.

this diverging behavior near the nematic region of the entropy landscape results from the singularity of  $\mathcal{D}(\epsilon_F)$ . As apparent in Eq. 26, at very low temperature only the states near the Fermi surfaces give a sizable contribution to the entropy. Since the nematic region is driven by the sudden increase of  $\mathcal{D}(\epsilon_F)$ , the entropy should also be enhanced near the nematic region. While it is generally expected that the quantum fluctuations near the critical point could contribute more entropies, our results demonstrate that entropy contributed from the mean-field level already gives diverging behavior due to the singularity of  $\mathcal{D}(\epsilon_F)$  under the evolution of the magnetic field.

To summarize, it is found that the singular behavior of  $\mathcal{D}(\epsilon_F)$  already produces diverging behavior in both entropy and specific heat under magnetic field at constant temperature, although the critical exponent  $\alpha$  can not be extracted from the current theory. Similar argument has been proposed in previous study<sup>34</sup>, in which the effect of a rigid band shift away from van Hove singularities in a perfect 1-d band is discussed. The quantum fluctuations seem to play a minor role in this case but become important in the vicinity of the quantum critical point and at higher temperature. It is noted that the rigid band picture does not work neither when the system is doped by the substitution of  $\text{La}^{3+}$  into the  $\text{Sr}^{2+}$  site, which has been argued to result from the strong correlation effect<sup>39</sup>. We will leave these discussions in the conclusion section.

### C. Total density of states

Iwaya *et al.* has measured the STM tunneling differential conductance  $\frac{dI}{dV}$  in the  $B$ -field for  $\text{Sr}_3\text{Ru}_2\text{O}_7$ , which corresponds to measurement of the DOS. It has been observed that while DOS at higher and lower energy does not change, the DOS at the Fermi energy ( $\mathcal{D}(\epsilon_F)$ ) in-

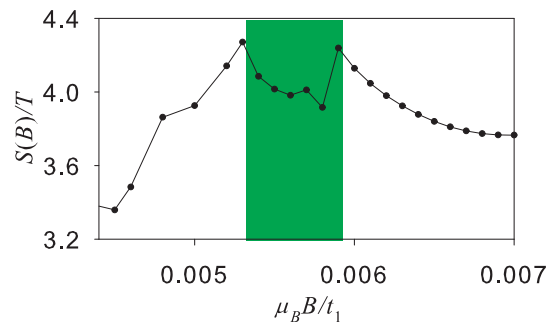


FIG. 4: (Color online) (a) The entropy landscape represented by the quantity  $S(B)/T$  in unit of  $k_B^2/t_1$  within the range of  $0.0045 \leq \mu_B B/t_1 \leq 0.007$ . A sudden increase near the nematic region (green area) is clearly seen.

crease significantly under the application of the magnetic field, demonstrating the violation of the rigid band picture.

In our model the total DOS can be evaluated using:

$$\rho_{tot}(\omega) = \frac{1}{\pi N} \sum_{\vec{k}}' \text{TrIm}[\hat{G}^{MF}(\vec{k}, \omega)]$$

$$\hat{G}^{MF}(\vec{k}, \omega) \equiv (\omega + i\eta - H^{MF}(\vec{k}))^{-1} \quad (27)$$

where  $H^{MF}(\vec{k})$  is given in Eq. 23 with the self-consistent order parameters and  $N$  is the total number of sites in the bilayer square lattices.

The profiles of the total DOS at several different magnetic field strength are plotted in Fig. 5(a), and clearly a rigid band picture does not apply here.  $\mathcal{D}(\epsilon_F)$  ( $\rho_{tot}(\omega = 0)$  in the plot) increases significantly as the nematic phase is approached. This feature can also be directly understood by the picture of Fermi surface reconstruction,



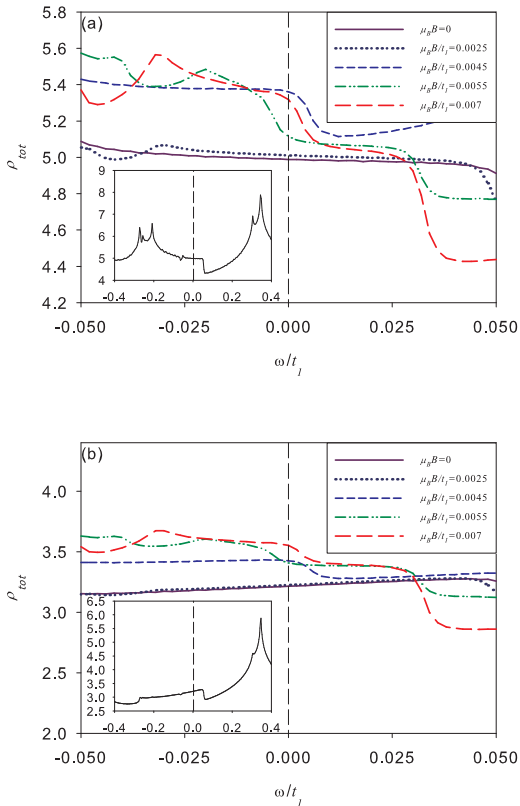


FIG. 5: (Color online) (a) The total DOS  $\rho_{tot}(\omega)$  as a function of  $\mu_B B$ . The broadening factor  $\eta$  is set to be  $\eta = 0.002t_1$ .  $\rho_{tot}(\omega)$  does not follow the rigid band picture and  $\rho_{tot}(\omega = 0)$  has a sudden increase near the nematic region. Inset: the total DOS at zero field for a wider range of  $|\omega|/t_1 \leq 0.4$ . The peaks corresponding to van Hove singularities are near  $\omega/t_1 \approx -0.2$  and  $\omega/t_1 \approx 0.35$ . (b) The DOS of the quasi-1D bands. Inset: the DOS of quasi-1D bands at zero field for a wider range of  $|\omega|/t_1 \leq 0.4$ . Only the peak around  $\omega/t_1 \approx 0.35$  remains, meaning that this peak is due to the van Hove singularities in quasi-1D bands.

since the changes in the Fermi surface topology inevitably lead to the non-monotonic behavior in  $\rho_{tot}(\omega = 0)$ . In particular, comparing Figs. 1 and 3, it is straightforward to see that more Fermi surfaces appear near the  $(\pm\pi, 0)$  and  $(0, \pm\pi)$  as the magnetic field increases. Since there are van Hove singularities near these four  $\vec{k}$  points,  $\rho_{tot}(\omega = 0)$  is expected to increase. As the magnetic field is increased further so that the van Hove singularities are all covered below the Fermi surfaces,  $\rho_{tot}(\omega = 0)$  starts to drop (not shown here).

At the first glance, the entropy measurement and our results of the total DOS seem to contradict with the STM measurement. While both the entropy measurement and our results develop a maximum around the nematic region in  $\mathcal{D}(\epsilon_F)$ , the STM measurement showed instead that  $\mathcal{D}(\epsilon_F)$  keeps increasing even after the nematic re-

gion is passed. To resolve this discrepancy, several realistic features need to be considered before comparing our calculations with the STM results. Since the STM is a surface probe and the surface of the material is usually cleaved to have the oxygen atoms in the outermost layer, there is an oxygen atom lying above each uppermost Ru atom. Consequently, the tunneling matrix element will be mostly determined by the wavefunction overlaps between the  $p$ -orbitals of the oxygen atom and the  $d$ -orbitals of the Ru atom, resulting in a much smaller matrix element for  $d_{xy}$  orbital compared to  $d_{xz,yz}$  orbitals<sup>18</sup>. The minimal model to take this effect into account is to extract the DOS only from the quasi-1D orbitals, which is plotted in Fig. 5(b). Although the overall profile in Fig. 5(b) is not exactly the same as that in Ref. 35, which is attributed to more complicated momentum dependence of tunneling matrix elements<sup>26,40,41</sup> not considered here, it captures the increasing DOS with the magnetic field which is more consistent with Ref. 35.

The insets in Fig. 5 plot the total and quasi-1D band DOSs at zero field within a wider range of  $|\omega|/t_1 \leq 0.4$ . The peaks corresponding to the van Hove singularities reside at  $\omega/t_1 \approx -0.2$  and  $\omega/t_1 \approx 0.35$ , far away from the Fermi energy. The reason why the small energy scale like Zeeman energy ( $\sim 0.003t_1$ ) can push the system to get closer to the van Hove singularities at energies far away from the Fermi energy is the help of the metamagnetism. In the mean-field theory, the magnetization produces an effective chemical potential shift as  $sUS_z^\alpha$  for electrons at orbital  $\alpha$  and spin  $s$ . As a result, under the magnetic field the jump in the magnetization gives  $S_z^\alpha \sim 0.05$  within the range of experimental interests. This leads to the effective chemical potential shift about  $\pm 0.18t_1$  for  $U = 3.6t_1$ , which is large enough to push the system closer to the van Hove singularities. This renormalization of the chemical potential by the interaction is also part of the cause for the violation of the rigid band picture.

#### D. Finite Temperature Phase Diagram

Another intriguing observation by Rost *et. al.*<sup>33</sup> is the phase boundary of the nematic phase at the finite temperature. Since the nematic phase is bounded by the two first-order metamagnetic transition, the phase boundary can be determined by the magnetic Clausius-Clapeyron relation:

$$\mu_0 \frac{dH_c}{dT_c} = -\frac{\Delta S}{\Delta M}, \quad (28)$$

where  $\mu_0$  is the permeability constant,  $H_c$  and  $T_c$  the critical field and temperature,  $S$  the entropy, and  $M = |\vec{\mathcal{M}}|$  the magnetization. Experimentally it was found that the entropy is always higher inside the nematic phase than the adjacent normal phases but the magnetization increases monotonically with the magnetic field. From Eq. 28, this implies a 'muffin'-shaped phase boundary, i.e., at field strengths slightly below  $7.8T$  and above  $8.1T$  the nematic phase appears at finite temperature but vanishes

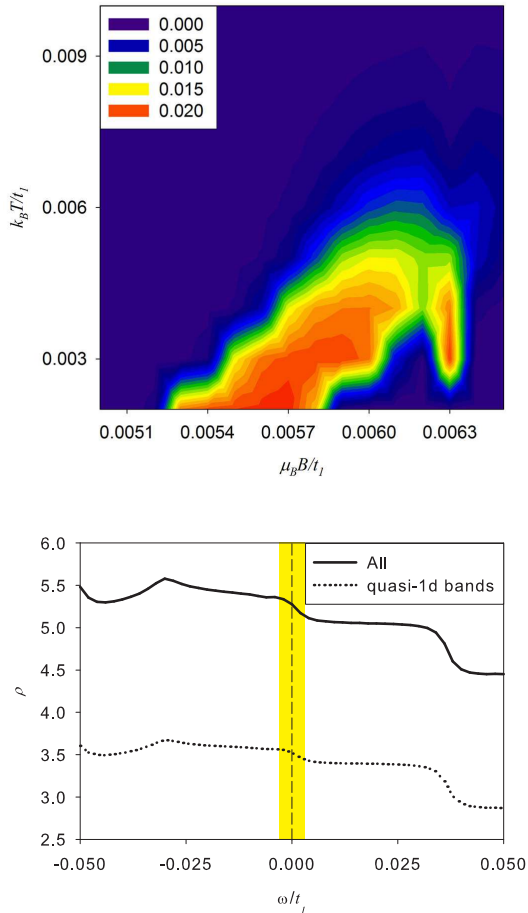


FIG. 6: (Color online) (a) Phase diagram for higher temperatures. Magnitudes of  $\mathcal{N}$  are represented by the color scales. The areas with light colors have large  $\mathcal{N}$ , defining the region for the nematic order. The re-entry of the nematic order at higher temperature is seen at fields between  $0.0058 < \mu_B B/t_1 < 0.0063$ . (b) The DOSs of the all bands (solid line) and quasi-1D bands (dashed line) at  $\mu_B B/t_1 = 0.006$ . The yellow areas refers to the energy window bounded by  $\pm k_B T/t_1$  with temperature  $k_B T/t_1 = 0.003$ . It can be seen that this thermal energy window covers a region in which the DOS increases abruptly, driving the nematic phase at finite temperature.

at zero temperature, to which we term as ‘re-entry’ behavior throughout this paper.

By inspecting Fig. 4 closer, it can be seen that the entropy drops as entering the nematic phase from the lower-field boundary but raises as entering from the upper-field boundary. In other words, the present theory has the ‘re-entry’ behavior of the nematic order at the upper-field boundary but not at the lower-field boundary. This aspect is further confirmed by the temperature dependence of the nematic order parameter  $\mathcal{N}$  as a function of magnetic field shown in Fig. 6(a).

The re-entry behavior can be understood as follow-

ing. Because the nematic phase transition is first-order, roughly speaking one requires  $U_{eff} \mathcal{D}(\epsilon_F)$ , where  $U_{eff}$  is the effective interaction for nematicity, to exceed a critical value for the nematic ordering to occur. The mechanism for nematic ordering in  $\text{Sr}_3\text{Ru}_2\text{O}_7$  based on van Hove singularities is all about increasing  $\mathcal{D}(\epsilon_F)$  abruptly by driving the system closer to the van Hove singularities with the magnetic field. At the field strength slightly above the upper critical field,  $\mathcal{D}(\epsilon_F)$  is large but still not enough for the occurrence of the nematic ordering. Therefore, if the thermal energy is large enough to cover enough DOS within the thermal energy window  $\epsilon_F - k_B T < \epsilon_F < \epsilon_F + k_B T$  but still low enough so that the thermal fluctuations are small, the re-entry of the nematic phase at higher temperature can be possible. As an illustration, Fig. 6(b) plots the DOS for  $\mu_B B/t_1 = 0.006$  at which the nematic ordering first occurs at  $k_B T/t_1 = 0.003$  in our calculation. It can be seen that the thermal energy window for  $k_B T/t_1 = 0.003$  (yellow areas) covers a region in which the DOS increases abruptly, consistent with the mechanism for the re-entry behavior discussed above.

## V. THE CASE OF THE TILTED MAGNETIC FIELDS ( $\theta \neq 0$ )

### A. $\theta$ dependence of the nematic ordering

Experimentally, it has been concluded from the magnetic susceptibility and resistivity measurements<sup>3,5,15</sup> that the resistive anisotropy disappears very quickly as the magnetic field is tilted away from the  $c$ -axis, suggesting that the nematic ordering vanishes with the increase of the field angle  $\theta$ . Fig. 7 presents the nematic order parameter  $\mathcal{N}$  as functions of  $\mu_B B$  and  $\theta$ . It should be noted that since the in-plane component of the orbital Zeeman energy explicitly break the  $C_4$  symmetry down to the  $C_2$  symmetry,  $\mathcal{N}$  is non-zero as long as  $\theta \neq 0$ . Nevertheless, the experimentally observable nematic phase can still be identified by the jumps in  $\mathcal{N}$ . Our results showed that the nematicity is strongly enhanced with the increase of  $\theta$ , which does not agree with the experiments.

The large enhancement of the nematic phase for  $\theta \neq 0$  in our calculation is due to the orbital Zeeman energy. The anisotropic in-plane component of the orbital Zeeman energy term  $-\mu_B B \sum_{i,a} L_{x,ia} \sin \theta$  is clearly proportional to  $B$  and largest at  $\theta = 90^\circ$  (i.e.  $\hat{B} \parallel \hat{x}$ ). To illustrate this point, we plot the Fermi surfaces without any interaction for  $\vec{B} \parallel \hat{x}$  with strength  $\mu_B |\vec{B}| = 0.1 t_1$  in Fig. 8, and an anisotropy can be seen. Although such anisotropy in the band structure is not important at low field, it can be amplified by the effect of the interactions, driving the system more susceptible to the nematic phase as the critical points is approached. As a result, the portion of the nematic phase in the phase diagram is enlarged as  $\theta$  increases from  $0^\circ$  to  $90^\circ$  as seen in our calculations. The disagreement between our the-



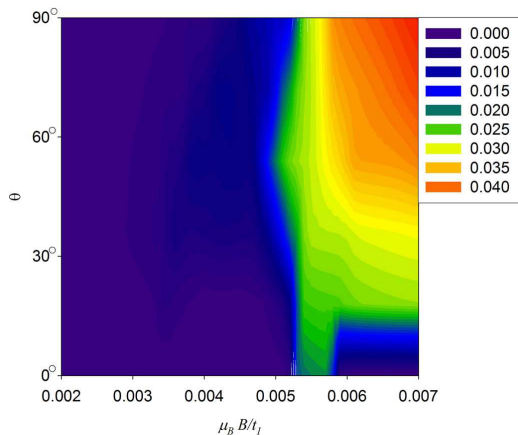


FIG. 7: (Color online) The nematic order parameter  $\mathcal{N}$  as functions of  $\mu_B B$  and  $\theta$ . The magnitudes of  $\mathcal{N}$  are represented by the color scales. For  $\theta \neq 0$ , the nematic order parameter is in general non-zero, but there is an area (with light colors) in which the nematic order parameter is sharply enhanced, defining the region of the nematic phase observed in experiments.

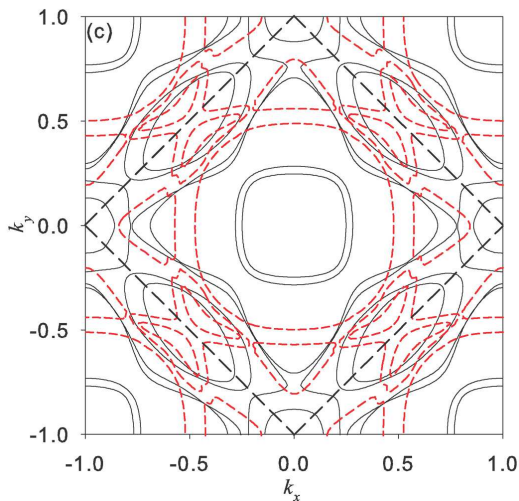


FIG. 8: (Color online) The non-interacting Fermi surfaces for  $\vec{B} \parallel \hat{x}$  and  $\mu_B B = 0.1t_1$ . The anisotropy in Fermi surfaces is already visible, especially for the areas near  $(\pm\pi, 0)$  and  $(0, \pm\pi)$ .

ory and the experimentally-determined phase diagram as a function of  $\theta$  could result from the strong correlation effect, which is beyond the scope of the mean-field theory.

### B. Anisotropy of the resistivity measurements

While it requires more experimental efforts to confirm the cause of disagreement, Raghu *et al.* have argued that the resistivity measurement might not be a good

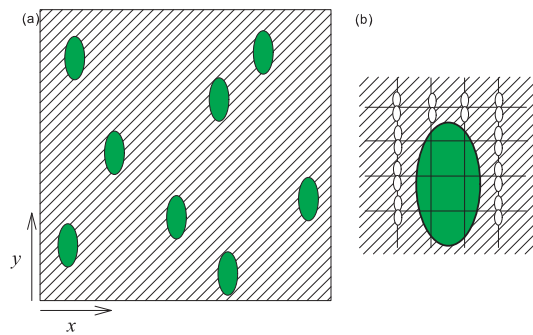


FIG. 9: (Color online) Illustration of the energetically-favored domain structures as the in-plane magnetic field is along  $\hat{x}$  axis. When the in-plane magnetic field is weak, orbital ordered phase with  $\mathcal{N} > 0$  are dominant (shaded areas) and high-energy domains with  $\mathcal{N} \leq 0$  (green ovals) could exist. (b) The domain walls extend longer in  $\hat{y}$  direction because it costs less energies if less  $\hat{y}$ - than  $\hat{x}$ - bonds are broken in a  $\mathcal{N} > 0$  background. The white oval represents the wave function of  $d_{yz}$  orbital on each site. The current flows much more easily along  $\hat{y}$ -axis than  $\hat{x}$ -axis since the electrons suffer less domain scatterings hopping along this direction. As the in-plane magnetic field is strong, these high-energy domains vanish, thus there is no longer an easy axis for the current flow.

indicator for the nematic phase in this material<sup>15</sup>. The point is that the nematic phase is mostly associated with the states near the van Hove singularity whose Fermi velocities are too small to have sizable contribution to the transport properties. Therefore the observed anisotropic resistivity is mostly likely due to the scatterings between nematic domains, and the tilt of the magnetic field helps lie up the domains. However, if the domains are fully lied up, the resistivity measurement becomes insensitive to the nematic phase due to the diminishing scatterings between nematic domains, despite the nematic order could be stronger.

One remaining puzzle of this domain scattering argument is why the easy axis for the current flow is perpendicular to the in-plane component of the  $B$ -field<sup>5</sup>. We provide a natural argument based on the anisotropic spatial extension of the domain walls as explained below. Assuming the  $B$ -field lying in the  $xz$ -plane, the in-plane ( $xy$ ) orbital Zeeman energy reads  $H_{in-plane} = -\mu_B B \sin \theta \sum_{i,a} L_{x,ia}$ , which couples the  $d_{xy}$  and  $d_{xz}$ -orbitals and breaks the degeneracy between the  $d_{xz}$  and  $d_{yz}$ -orbitals. Since the  $d_{xy}$ -orbital has lower on-site energy due to the crystal field splitting than that of  $d_{xz}$ , the  $d_{xz}$ -orbital bands are pushed to higher energy than  $d_{yz}$ -orbital bands by this extra coupling. As a result, the nematic state with preferred  $d_{yz}$ -orbitals (i.e.,  $\mathcal{N} > 0$ ) has lower energy in the homogeneous system. At small angles of  $\theta$ , domains with preferred  $d_{xz}$ -orbitals (i.e.  $\mathcal{N} \leq 0$ ) could form as depicted in Fig. 9 (a) as meta-stable states, which occupy less volume than the majority domain of  $\mathcal{N} > 0$ . Let us consider the shape of the domain walls. Because of the quasi-1D features of the  $d_{xz}$  and

$d_{yz}$ -orbitals, the horizontal (vertical) domain wall breaks the bonds of the  $d_{yz}(d_{xz})$ -orbital as depicted in Fig. 9 (b), respectively. Since the  $d_{yz}$ -orbital is preferred by  $H_{in-plane}$ , the horizontal domain wall costs more energy. Consequently, the domain structure illustrated in Fig. 9 (a) with longer vertical walls than the horizontal walls is energetically favored.

Since the electrons suffer less domain scatterings hopping along the  $\hat{y}$ -axis in this domain structure, it becomes the easy axis for the current flow. At large values of  $\theta$ , higher energy domains are suppressed and eventually vanish, and thus the resistivity measurement becomes insensitive to the nematic phase because of vanishing of the domain scatterings.

### C. Measurements proposed for the nematicity

Our results have posted a possibility that the nematic order could occur in a larger range of the magnetic field for  $\vec{B} \parallel \hat{x}$  than for  $\vec{B} \parallel \hat{z}$ . Detection methods other than resistivity would be desirable. One feasible way is to measure the quasiparticle interference (QPI) in the spectroscopic imaging STM which has been examined in detail in our previous work<sup>18</sup>. It has been predicted by us that if there is a nematic order, QPI spectra will manifest patterns breaking rotational symmetry.

Another possible experiment is the nuclear quadruple resonance (NQR) measurement, which has been widely used to reveal ordered states in high- $T_c$  cuprates<sup>42-44</sup> and recently the iron-pnictides<sup>45</sup>. This technique utilizes the feature that a nucleus with a nuclear spin  $I \geq 1$  has a non-zero electric quadruple moment. Because the electric quadruple moment creates energy splittings in the nuclear states as a electric field gradient is present, a phase transition could be inferred if substantial changes in the resonance peak are observed in the NQR measurement. Besides, since this is a local probe at the atomic level, it is highly sensitive to the local electronic change. Given that Ru atom has a nuclear spin of  $I = 5/2$ <sup>46</sup> and the orbital ordering in the quasi-1D bands significantly changes the charge distribution around the nuclei, a systematic NQR measurement as functions of magnetic field and field angle will reveal more conclusive information about nematicity.

## VI. CONCLUSIONS

In this paper we have shown that a number of important properties observed in the bilayer  $\text{Sr}_3\text{Ru}_2\text{O}_7$  could be qualitatively consistent with a realistic tight-binding model together with on-site interactions treated at mean-field level. The band structure of this material is complicated by multibands, bilayer splitting, rotations of RuO octahedra, and the spin-orbit coupling, collectively leading to the high sensitivity to the small energy scales. This

is the main cause of the singular behavior in the evolution of the Fermi surfaces under magnetic field. Using our tight-binding model and the standard mean-field approaches on the intra- and inter- orbital Hubbard interactions, we find that for the case of magnetic field parallel to the  $c$ -axis, the nematic order, which is interpreted as the orbital ordering in quasi-1d  $d_{yz}$  and  $d_{xz}$  bands, appears at the magnetic field at the same order of the experimental values  $\sim 8\text{T}$ . Moreover, we find that the total density of states at the Fermi energy  $\mathcal{D}(\epsilon_F)$  under the magnetic field does not follow a rigid band picture, in agreements with the results of STM measurement<sup>35</sup>.

The failure of following a rigid band picture is essentially a consequence of the interplay between spin-orbit coupling and the Zeeman energy, despite the strong correlation effect could also result in the violation of the rigid band shift upon doping<sup>39</sup>. Because the spin-orbit coupling hybridizes the quasi-1D bands and 2-D bands with *opposite* spins, the Zeeman energy naturally induces the reconstruction of the Fermi surfaces instead of just rigid chemical potential shifts. This singular behavior in  $\mathcal{D}(\epsilon_F)$  also results in the divergences in the entropy and specific heat landscapes, since at very low temperature both quantities are approximately proportional to  $\mathcal{D}(\epsilon_F)$ . Because the divergence observed by Rost *et. al.*<sup>33</sup> start approximately at 6-7 Tesla which is not very close to the quantum critical point residing about 8 Tesla, a direct application of the quantum critical scaling seems to be inappropriate. The explanation of the critical exponent associated with this divergence could not be complete without taking the band structure singularity into account in this particular material<sup>21</sup>.

As the magnetic field is tilted away from the  $c$  axis ( $\theta \neq 0$ ), we find that nematic region expands instead of shrinking as the resistivity measurement has indicated. From the theoretical viewpoints, the tilt of the magnetic field induces an extra in-plane component of the orbital Zeeman energy which explicitly breaks the  $C_4$  symmetry down to the  $C_2$  symmetry. As argued above that this system is very sensitive to small energy scale, the effect of this extra Zeeman energy is not important at low field but could amplify the effect of interaction to drive the system toward nematicity as the quantum critical point is approached. As a result, the nematic phase is more favored and stable in the presence of the in-plane magnetic field and it requires another Fermi surface reconstruction at even higher magnetic field in order to weaken the nematic phase by reduced  $\mathcal{D}(\epsilon_F)$ .

To explain this discrepancy between our theory and the resistivity measurement, we adopt the domain scattering argument proposed by Raghu *et. al.*<sup>15</sup>. Furthermore, we have given an explanation for another experimental puzzle that the easy axis for the current flow is always perpendicular to the in-plane magnetic field. Measurements like quasiparticle interference in the spectroscopic imaging STM and NQR which could detect the orbital ordering directly have been proposed to be more reliable probes for the nematicity in this material than the resis-

tivity measurement.

Finally we would like to comment on limitation of the present theory. Although we have found the 're-entry' behavior of the nematic phase, i.e., the appearance of the nematic phase only at the finite temperature but not at the zero temperature, near the upper-field boundary, the experiments showed this behavior near both upper- and lower- field boundary. In our calculations, the re-entry behavior is due to the increase of the density of states within the narrow energy window around the Fermi energy opened by thermal energy, but we do not reject other schemes for the re-entry behavior. One possible scheme is an analogue of ferromagnetism without exchange splitting proposed by Hirsch<sup>47</sup>. He showed that the nearest neighbor interactions could result in a spin-dependent renormalization on the bandwidth (equivalently, the effective mass). As a result, the filling for different spin bands can be different because of the unequal effective masses, leading to the ferromagnetism even without the exchange splitting as in the Stoner model.

In Hirsch's original paper, the re-entry of the ferromagnetism at higher temperature was found. Since we only considered the on-site interactions in our model, such an effect is beyond the scope of the current theory. It is possible that after including the nearest neighbor interaction, the renormalizations of the bandwidths have

novel temperature-dependences, leading to a phase diagram better consistent with the experiments. If this is the correct scheme, the re-entry of the nematic states should be accompanied by a change in the kinetic energy due to the effective mass renormalization, which could be examined by the sum rules for the optical properties<sup>47-51</sup>.

Another possible scheme for the re-entry behavior is the quantum critical fluctuations. It is well-known that the influences of the critical fluctuations extend from the quantum critical point to finite temperature in a V-shape region in the phase diagram. Moreover, the critical fluctuations in this material contain not only the ferromagnetic but also the nematic ones. As a result, it is not surprising that the competition between these two types of critical fluctuations leads to an intriguing phase diagram at the finite temperature, and the study toward this direction is currently in progress.

## VII. ACKNOWLEDGMENT

We thank J. E. Hirsch and A. Mackenzie for valuable discussions. C. W. and W. C. L. are supported by ARO-W911NF0810291 and Sloan Research Foundation.

- 
- \* Electronic address: leewc@physics.ucsd.edu  
 † Electronic address: wucj@physics.ucsd.edu
- <sup>1</sup> S. A. Grigera, R. S. Perry, A. J. Schofield, M. Chiao, S. R. Julian, G. G. Lonzarich, S. I. Ikeda, Y. Maeno, A. J. Millis, and A. P. Mackenzie, *Science* **294**, 329 (2001).
  - <sup>2</sup> R. S. Perry, L. M. Galvin, S. A. Grigera, L. Capogna, A. J. Schofield, A. P. Mackenzie, M. Chiao, S. R. Julian, S. I. Ikeda, S. Nakatsuji, et al., *Phys. Rev. Lett.* **86**, 2661 (2001).
  - <sup>3</sup> S. A. Grigera, R. A. Borzi, A. P. Mackenzie, S. R. Julian, R. S. Perry, and Y. Maeno, *Phys. Rev. B* **67**, 214427 (2003).
  - <sup>4</sup> S. A. Grigera, P. Gegenwart, R. A. Borzi, F. Weickert, A. J. Schofield, R. S. Perry, T. Tayama, T. Sakakibara, Y. Maeno, A. G. Green, et al., *Science* **306**, 1154 (2004).
  - <sup>5</sup> R. A. Borzi, S. A. Grigera, J. Farrell, R. S. Perry, S. J. S. Lister, S. L. Lee, D. A. Tennant, Y. Maeno, and A. P. Mackenzie, *Science* **315**, 214 (2007).
  - <sup>6</sup> A. J. Millis, A. J. Schofield, G. G. Lonzarich, and S. A. Grigera, *Phys. Rev. Lett.* **88**, 217204 (2002).
  - <sup>7</sup> A. G. Green, S. A. Grigera, R. A. Borzi, A. P. Mackenzie, R. S. Perry, and B. D. Simons, *Phys. Rev. Lett.* **95**, 086402 (2005).
  - <sup>8</sup> H.-Y. Kee and Y. B. Kim, *Phys. Rev. B* **71**, 184402 (2005).
  - <sup>9</sup> H. Yamase and A. Katanin, *J. Phys. Soc. Japan* **76**, 073706 (2007).
  - <sup>10</sup> H. Yamase, *Phys. Rev. B* **76**, 155117 (2007).
  - <sup>11</sup> C. Puetter, H. Doh, and H.-Y. Kee, *Phys. Rev. B* **76**, 235112 (2007).
  - <sup>12</sup> A. M. Berridge, A. G. Green, S. A. Grigera, and B. D. Simons, *Phys. Rev. Lett.* **102**, 136404 (2009).
  - <sup>13</sup> A. M. Berridge, S. A. Grigera, B. D. Simons, and A. G. Green, *Phys. Rev. B* **81**, 054429 (2010).
  - <sup>14</sup> W.-C. Lee and C. Wu, *Phys. Rev. B* **80**, 104438 (2009).
  - <sup>15</sup> S. Raghu, A. Paramekanti, E. A. Kim, R. A. Borzi, S. A. Grigera, A. P. Mackenzie, and S. A. Kivelson, *Phys. Rev. B* **79**, 214402 (2009).
  - <sup>16</sup> C. M. Puetter, J. G. Rau, and H.-Y. Kee, *Phys. Rev. B* **81**, 081105 (2010).
  - <sup>17</sup> M. H. Fischer and M. Sigrist, *Phys. Rev. B* **81**, 064435 (2010).
  - <sup>18</sup> W.-C. Lee, D. P. Arovas, and C. Wu, *Phys. Rev. B* **81**, 184403 (2010).
  - <sup>19</sup> C. Wu, D. Bergman, L. Balents, and S. D. Sarma, *Phys. Rev. Lett.* **99**, 70401 (2007).
  - <sup>20</sup> A. Tamai, M. P. Allan, J. F. Mercure, W. Meevasana, R. Dunkel, D. H. Lu, R. S. Perry, A. P. Mackenzie, D. J. Singh, Z.-X. Shen, et al., *Phys. Rev. Lett.* **101**, 026407 (2008).
  - <sup>21</sup> J. Lee, M. P. Allan, M. A. Wang, J. Farrell, S. A. Grigera, F. Baumberger, J. C. Davis, and A. P. Mackenzie, *Nat. Phys.* **5**, 800 (2009).
  - <sup>22</sup> M. B. Salamon and M. Jaime, *Rev. Mod. Phys.* **73**, 583 (2001).
  - <sup>23</sup> G. Khaliullin, *Prog. Theor. Phys. Suppl.* **160**, 155 (2005).
  - <sup>24</sup> J. Zhao, D. T. Adroja, D.-X. Yao, R. Bewley, S. Li, X. F. Wang, G. Wu, X. H. Chen, J. Hu, , et al., *Nat. Phys.* **5**, 555 (2009).
  - <sup>25</sup> T.-M. Chuang, M. P. Allan, J. Lee, Y. Xie, N. Ni, S. L. Bud'ko, G. S. Boebinger, P. C. Canfield, and J. C. Davis, *Science* **327**, 181 (2010).
  - <sup>26</sup> W.-C. Lee and C. Wu, *Phys. Rev. Lett.* **103**, 176101

- (2009).
- <sup>27</sup> W. Lv, F. Krüger, and P. Phillips, *Phys. Rev. B* **82**, 045125 (2010).
- <sup>28</sup> C. Chen, J. Maciejko, A. P. Sorini, B. Moritz, R. R. P. Singh, and T. P. Devereaux, arXiv.org:1004.4611 (2010).
- <sup>29</sup> P. Coleman and A. J. Schofield, *Nature* **433**, 226 (2005).
- <sup>30</sup> H. v. Löhneysen, A. Rosch, M. Vojta, and P. Wölfle, *Rev. Mod. Phys.* **79**, 1015 (2007).
- <sup>31</sup> J. A. Hertz, *Phys. Rev. B* **14**, 1165 (1976).
- <sup>32</sup> A. J. Millis, *Phys. Rev. B* **48**, 7183 (1993).
- <sup>33</sup> A. W. Rost, R. S. Perry, J.-F. Mercure, A. P. Mackenzie, and S. A. Grigera, *Science* **325**, 1360 (2009).
- <sup>34</sup> A. W. Rost, A. M. Berridge, R. S. Perry, J.-F. Mercure, S. A. Grigera, and A. P. Mackenzie, *Phys. Status Solidi B* **247**, 513 (2010).
- <sup>35</sup> K. Iwaya, S. Satow, T. Hanaguri, N. Shannon, Y. Yoshida, S. I. Ikeda, J. P. He, Y. Kaneko, Y. Tokura, T. Yamada, et al., *Phys. Rev. Lett.* **99**, 057208 (2007).
- <sup>36</sup> D. Singh and I. Mazin, *Phys. Rev. B* **63**, 165101 (2001).
- <sup>37</sup> A. Liebsch and A. Lichtenstein, *Phys. Rev. Lett.* **84**, 1591 (2000).
- <sup>38</sup> I. Eremin, D. Manske, and K. Bennemann, *Phys. Rev. B* **65**, 220502 (2002).
- <sup>39</sup> J. Farrell, R. S. Perry, A. Rost, J. F. Mercure, N. Kikugawa, S. A. Grigera, and A. P. Mackenzie, *Phys. Rev. B* **78**, 180409 (2008).
- <sup>40</sup> J. Tersoff and D. Hamann, *Phys. Rev. Lett.* **50**, 1998 (1983).
- <sup>41</sup> Y. Zhang, V. W. Brar, F. Wang, C. Girit, Y. Yayon, M. Panlasigui, A. Zettl, and M. F. Crommie, *Nat. Phys.* **4**, 627 (2008).
- <sup>42</sup> P. C. Hammel, B. W. Statt, R. L. Martin, F. C. Chou, D. C. Johnston, and S.-W. Cheong, *Phys. Rev. B* **57**, R712 (1998).
- <sup>43</sup> G. B. Teitelbaum, B. Büchner, and H. de Gronckel, *Phys. Rev. Lett.* **84**, 2949 (2000).
- <sup>44</sup> P. M. Singer, A. W. Hunt, and T. Imai, *Phys. Rev. Lett.* **88**, 047602 (2002).
- <sup>45</sup> G. Lang, H.-J. Grafe, D. Paar, F. Hammerath, K. Manthey, G. Behr, J. Werner, and B. Büchner, *Phys. Rev. Lett.* **104**, 097001 (2010).
- <sup>46</sup> K. Ishida, Y. Kitaoka, K. Asayama, S. Ikeda, S. Nishizaki, Y. Maeno, K. Yoshida, and T. Fujita, *Phys. Rev. B* **56**, R505 (1997).
- <sup>47</sup> J. E. Hirsch, *Phys. Rev. B* **59**, 6256 (1999).
- <sup>48</sup> Y. Okimoto, T. Katsufuji, T. Ishikawa, A. Urushibara, T. Arima, and Y. Tokura, *Phys. Rev. Lett.* **75**, 109 (1995).
- <sup>49</sup> Y. Okimoto, T. Katsufuji, T. Ishikawa, T. Arima, and Y. Tokura, *Phys. Rev. B* **55**, 4206 (1997).
- <sup>50</sup> D. N. Basov and T. Timusk, *Rev. Mod. Phys.* **77**, 721 (2005).
- <sup>51</sup> A. D. LaForge, W. J. Padilla, K. S. Burch, Z. Q. Li, A. A. Schafgans, K. Segawa, Y. Ando, and D. N. Basov, *Phys. Rev. Lett.* **101**, 097008 (2008).